

See discussions, stats, and author profiles for this publication at: <https://www.researchgate.net/publication/269910852>

Synthesis, Characterization, and Formation Mechanism of Crystalline Cu and Ni Metallic Nanowires under Ambient, Seedless, Surfactantless Conditions

ARTICLE *in* CRYSTAL GROWTH & DESIGN · AUGUST 2014

Impact Factor: 4.89 · DOI: 10.1021/cg500324j

CITATION

1

READS

27

5 AUTHORS, INCLUDING:



[Crystal S. Lewis](#)

Stony Brook University

4 PUBLICATIONS 2 CITATIONS

SEE PROFILE



[Lei Wang](#)

Stony Brook University

14 PUBLICATIONS 43 CITATIONS

SEE PROFILE



[Haiqing Liu](#)

Stony Brook University

15 PUBLICATIONS 89 CITATIONS

SEE PROFILE



[Jinkyu Han](#)

Brookhaven National Laboratory

16 PUBLICATIONS 12 CITATIONS

SEE PROFILE

Synthesis, Characterization, and Formation Mechanism of Crystalline Cu and Ni Metallic Nanowires under Ambient, Seedless, Surfactantless Conditions

Crystal S. Lewis,[†] Lei Wang,[†] Haiqing Liu,[†] Jinkyu Han,[‡] and Stanislaus S. Wong^{*,†,‡}

[†]Department of Chemistry, State University of New York at Stony Brook, Stony Brook, New York 11794-3400, United States

[‡]Condensed Matter Physics and Materials Sciences Department, Brookhaven National Laboratory, Building 480, Upton, New York 11973, United States

Supporting Information

ABSTRACT: In this report, crystalline elemental Cu and Ni nanowires have been successfully synthesized through a simplistic, malleable, solution-based protocol involving the utilization of a U-tube double diffusion apparatus under ambient conditions. The nanowires prepared within the 50 and 200 nm template membrane pore channels maintain diameters ranging from ~90–230 nm with lengths attaining the micrometer scale. To mitigate for the unwanted but very facile oxidation of these nanomaterials to their oxide analogues, our synthesis mechanism relies on a carefully calibrated reaction between the corresponding metal precursor solution and an aqueous reducing agent solution, resulting in the production of pure, monodisperse metallic nanostructures. These as-prepared nanowires were subsequently characterized from an applications' perspective so as to investigate their optical and photocatalytic properties.



■ INTRODUCTION

Nanomaterials, referring to structures with at least one feature size between 1 and 100 nm, have attracted significant research interest due to their unique size-dependent optical, magnetic, electronic, thermal, mechanical, and chemical properties as compared with those of the corresponding bulk material. Specifically, metallic nanostructures exhibit unique optical and electronic properties as a result of their strong plasmonic resonance bands in the visible region, the delocalization of conduction electrons at the nanoscale, as well as an increasing binding energy with correspondingly decreasing size regimes.^{1,2} This scenario causes electrons in these materials to potentially undergo quantum confinement effects, thereby exhibiting comparable behavior with those of quantum dots, and these nanostructures often exhibit poor electron screening, as manifested in observed size-dependent metal–insulator transitions.^{1,3–6} As a result, applications involving these nanostructures include but are not limited to electronic devices, catalysts, and photocatalysts.^{7,8}

Copper (Cu) has been universally used in practical products, such as electrical devices, water pipes, roofing materials, and brass furnishings. Moreover, copper for electronics has made a huge impact upon technology, since it is an excellent conductor for heat and electricity. Copper-containing nanostructures have generated significant interest, due to the metal's earth abundance, and have been extensively analyzed at the nanoscale in order to probe their potentially game-changing thermal and electrical conductivities.^{9,10} Currently, films derived from copper nanowires (Cu NWs) produced from aqueous

solution-based protocols have achieved respectable optoelectronic performance, characterized by a sheet resistance of 61 ohm/cm² and 67% transmittance.¹¹ It was found that this device performance can be tuned by varying the concentration of the Cu NW ink. Corresponding films composed of electrospun Cu NWs have been shown to possess very low resistance and high transmittance properties, while maintaining mechanical flexibility.¹² Not surprisingly, research has been initiated on Cu NWs for a variety of applications including but not limited to solar cells,^{13,14} touch screens, and light-emitting diodes.^{15–18}

Similarly, nickel (Ni) is commonly used for the production of stainless steel, due to the metal's favorable resistance to high temperature and corrosion.¹⁹ It has also been used in the past as rechargeable batteries and as catalysts.^{20–22} Specifically, for rechargeable batteries, due to the low solubility product constant ($K_{sp} = 10^{-35}$ M) of its hydroxide form, nickel oxide-based batteries are able to hold more energy and maintain stability under commercial cycle durability conditions, ranging from 500 to 1000 cycles.^{23,24} Ni NWs are also widely known for their electrical transport properties and have been found to show a similar but larger magnitude of temperature-dependent resistivity as compared with bulk Ni. This observation may potentially be ascribed to the presence of either grain boundary

Received: March 5, 2014

Revised: June 8, 2014

Published: June 26, 2014



scattering or defects within the crystal structure at the nanoscale.²⁵

Recently, high-quality metal one-dimensional (1D) nanostructures, such as nanowires or nanotubes, have been considered as novel systems for their potential applications in sensing, electronic, and optical devices due to their high surface area-to-volume ratio.²⁶ Many different approaches for the preparation of these coinage metal nanomaterials (such as Cu and Ni) include but are not limited to electrospinning, electrochemical deposition, UV photolithography, hydrothermal processes, liquid phase reduction, and chemical vapor deposition (CVD) methods.^{9,27–45} However, while these techniques can successfully generate these nanomaterials, a step forward synthetically speaking would be to possibly mitigate for the use of specialized instrumentation (e.g., lithography), high energy processing (e.g., CVD), or potentially toxic precursors (i.e., hydrazine in conventional wet chemistry protocols) in order to synthesize pure, monodisperse, and crystalline Cu or Ni nanostructures.

In other words, it would be desirable if these nanostructures could be produced in as little as a few hours under ambient temperature and pressure conditions, using only relatively mild precursors that would react completely without the need for any extraneous reagents or catalysts. In this context, our laboratory has successfully achieved 1D nanowires of various materials, including metal oxides (i.e., ZnO, CuO, Fe₂O₃, BaCrO₄, CaWO₄, SrWO₄, MnWO₄, and BaWO₄ as well as their doped analogues), metal sulfides (i.e., CdS, PbS, and CuS), metal fluorides (i.e., BaF₂, CaF₂, SrF₂, KMnF₃, and NH₄MnF₃), metal phosphates (i.e., Tb-doped CePO₄), pure elemental metals (i.e., Au, Ag, Pt, and Pd), and homogeneous segmented binary materials (i.e., Pd/Au and Pd/Pt) using a reasonably simple protocol.^{46–54} This method consists of using the two arms of a glass U-tube apparatus to initiate and promote a solution-based, double-diffusion process to account for nanowire synthesis under ambient room-temperature conditions. Specifically, the well-defined channel pores of either alumina or polymer templates are used as spatially confined reaction media to control and define either nanotube or nanowire growth, respectively.

Over the years, we have noted that such a methodology does not require either (1) high temperatures or high-energy inputs, (2) powered instrumentation, or (3) an association with particularly toxic reagents/byproducts. For metal nanowires (i.e., Cu and Ni, in particular), which (i) tend to oxidize relatively easily, (ii) are difficult to form as a pure motif, and (iii) are therefore particularly sensitive to the reaction conditions used to create them, we note that the same solution-based template methodology can be applied with the use of commercially available and relatively inexpensive sodium borohydride (NaBH₄) as the reducing agent, due to its standard reduction potential value (−1.24 V), which is capable of readily reducing Cu²⁺ (0.34 V) and Ni²⁺ (−0.25 V) at room temperature.⁵⁵ Such a strategy therefore provides a relatively low cost, flexible, and generalizable approach for synthesizing these nanowires under ambient conditions. The size and morphology regime of these nanomaterials can be reliably varied and altered by controlling the template pore size and thickness from whence these nanowires are ultimately isolated.

■ EXPERIMENTAL SECTION

Synthesis. Polycarbonate (PC) membranes, measuring 6 μm in thickness with track etched channels maintaining pore size diameters

of 50 and 200 nm, respectively, were purchased from Fisher Scientific. Initially, these membranes were immersed in distilled water and subsequently ultrasonicated to ensure removal of air bubbles either within or on the top of the surfaces of the membranes. The PC membrane was then placed between the two half-cells of a custom-made glass U-tube apparatus. To synthesize Cu NWs, an aqueous solution of freshly prepared 0.05 M NaBH₄ under basic conditions (i.e., 0.05 M, sodium hydroxide, NaOH) was filled in one arm of the U-tube, and a corresponding solution of 0.05 M CuCl₂ was inserted into the other arm, simultaneously, in order to induce Cu nanowire growth. A full summary of all reactions used to generate as-prepared Cu nanowires, including an accompanying description of the results of a systematic parameter variation, is described in Table S1 and Figures S1–S6, Supporting Information. With Cu, we expended most of our efforts on testing the effects of using different reaction variables using the smaller 50 nm templates, as these gave uniformly better results.

As for the analogous Ni NWs, corresponding solutions of 0.05 M NaBH₄ and 0.1 M nickel chloride (NiCl₂) were prepared in ethanol (since most nickel nanomaterials are prepared in this solvent) and placed in the arms of the U-tubes using 50 nm template membranes to generate corresponding ~50 nm diameter nanowires.³⁸ With Ni, we probed the effect of varying template pore size. Hence, as for the larger nanowires prepared from 200 nm template membrane pores, solutions of 0.05 M NiCl₂ and 0.05 M NaBH₄ in ethanol were used to initiate the nanowire growth reaction.

The ostensible localized differences in reagent concentrations in these experiments were determined by the diffusion rates of each precursor within the PC template membrane pores themselves. The U-tube was subsequently left undisturbed for 2 h at room temperature. After the U-tube was dismantled, the template membrane was collected, placed onto a smoothing stone, and lubricated with mineral oil in order to ensure the physical removal of the bulk metal residual backing (i.e., a silver hue for Ni nanowires and a corresponding bronze color for Cu nanowires) on the external template surface. An image of a typical metal backing associated with Cu nanowires is shown in Figure S6. The corresponding summary of all reactions used to generate as-prepared Ni nanowires, including the results of a systematic parameter variation, is shown in Table S2, and the data are supported with Figures S7 and S8.

Once the excess reaction residue was eliminated, the template was then dissolved in dichloromethane for an hour, washed, and centrifuged several times for further purification. After processing, both types of metallic NWs were stored in oleylamine in order to prevent oxidation and isolated using a solution containing a 3:1 ratio of toluene and ethanol for further structural characterization. Residual salt content (i.e., NaCl) was removed from the Ni NWs through washing using an aqueous solution composed of a 1:1 ratio of deionized water to ethanol.

Photocatalytic Degradation Experiments. (a) *Cu NWs.* The Cu NWs were immobilized onto oleic acid capped TiO₂ nanoparticles (NPs) using a previously reported literature protocol with quantities of TiO₂ approaching 30 wt %.⁵⁶ As-prepared TiO₂ NPs were synthesized hydrothermally using an existing technique developed in our laboratory, and particle size distributions measured 15 ± 7 nm.⁵⁷ For each photodegradation experiment, 10 mg of the resulting Cu NW-TiO₂ heterostructures, as-prepared TiO₂ NPs, and a bulk Cu sample were added to aqueous solutions of Methyl Orange dye (MO, 10 mg/L) in independent runs.⁵⁶ MO dye was preferentially chosen as a result of its resonance peak at ~450 nm, which is located near the corresponding absorption maximum of Cu NW-TiO₂ heterostructures. The mixture was subsequently stirred at room temperature and irradiated at 366 nm (~3.4 eV) excitation, using an Entela UVGL-S8 mineralight UV lamp (operating at 115 V, ~60 Hz, and 0.16 A). At 15 min intervals, aliquots of the reaction mixture were removed, centrifuged, and isolated. Absorbance values were recorded in the absence of NPs at 450 nm using a UV1 UV–visible spectrophotometer (Thermo Scientific).

(b) *Ni NWs.* The Ni NWs were also attached onto our hydrothermally processed TiO₂ NPs using the same literature protocol with TiO₂ quantities approaching 30 wt %.⁵⁶ For each independent

photodegradation experiment, 10 mg of Ni NW-TiO₂ heterostructures, as-prepared TiO₂, and a bulk Ni sample were respectively added to aqueous solutions of Methylene Blue dye (MB, 50 mM).⁵⁸ This dye was chosen due to its characteristic absorption profile within the visible region. The mixture was subsequently stirred in the dark for 30 min and then illuminated under ambient fluorescent white light conditions for an additional 2 h. At 30 min intervals, aliquots of the mixture were systematically removed and centrifuged, prior to recording of the absorbance values at $\lambda = 664$ nm (~ 1.87 eV), i.e., the dye maximum.

Characterization. As-prepared samples were characterized using various techniques, such as powder X-ray diffraction (XRD), field-emission scanning electron microscopy (FE-SEM), transmission electron microscopy (TEM), high-resolution TEM (HR-TEM), selected area electron diffraction (SAED), energy-dispersive X-ray spectroscopy (EDS), electron energy loss spectroscopy (EELS) cross-sectional analysis, and UV–visible spectroscopy.

X-ray Diffraction (XRD). Crystallographic and purity of as-prepared NWs were confirmed using powder XRD. To prepare a typical sample for analysis, a fixed quantity was dispersed in ethanol and sonicated for ~ 1 min, prior to deposition onto a glass slide. Diffraction patterns were then obtained using a Scintag diffractometer, operating in the Bragg configuration using Cu K α radiation ($\lambda = 1.54$ Å) and 2θ lattice parameters ranging from 30 to 80° at a scanning rate of 0.25°/min for both Cu NWs and Ni NWs.

Electron Microscopy. The morphology and size of the metal nanowires were observed using a field emission SEM (FE-SEM Leo 1550) and an analytical high resolution SEM (JEOL 7600F) instrument at an accelerating voltage of 15 kV, both of which were equipped with EDS capabilities. To prepare these samples for characterization, fixed amounts were dispersed in ethanol and sonicated for ~ 1 min, prior to deposition onto a silicon (Si) wafer.

Low magnification TEM was also used at an accelerating voltage of 120 kV on the JEOL JEM-1400 instrument, with a 2048 \times 2048 Gatan CCD digital camera. High-resolution HR-TEM images coupled with SAED patterns were recorded using a JEOL JEM-3000F microscope, equipped with a Gatan image filter (GIF) spectrometer at an accelerating voltage of 300 kV. Electron energy loss spectroscopy (EELS) data, in combination with scanning transmission electron microscopy, were taken at an accelerating voltage of 200 kV on a JEOL JEM-2100F microscope using a Gatan Tridiem energy imaging filter. Specifically, spectra were collected with a spectrometer-defined dispersive resolution of 0.5 eV/channel. Both samples were prepared for analysis by dispersion in ethanol followed by sonication. Subsequently, the solution was deposited dropwise onto a 300 mesh Cu grid.

Optical Spectroscopy. UV–visible spectra were obtained at high resolution with a UV1 UV–visible spectrophotometer (Thermo Scientific) using quartz cells possessing a 10 mm path length. Specifically, the metallic NWs were sonicated in ethanol to yield a relatively clear (i.e., a reddish brown color for Cu NWs and a black hue for Ni NWs), homogeneous mixture. The mixture was then added to the quartz cell and the subsequent UV–visible spectra were recorded using ethanol as a blank.

RESULTS AND DISCUSSION

(i). X-ray Diffraction. The purity and crystallinity of our as-prepared NWs were characterized using XRD, as shown in Figure 1, panels A and B for the Cu and Ni samples, respectively. All diffraction peaks present could be readily indexed to the JCPDS 04-0836 for face centered cubic (fcc) crystalline Cu; there are only additional 2 diminutive peaks, situated at 2θ values of 38° and 39°, respectively, consistent with the formation of copper(I) oxide (Cu₂O), as described by JCPDS #33-0451. This impurity may be ascribed to the exposure of the NWs to oxygen during the 4-hour scanning time, a hypothesis that is also consistent with the prior literature in that it is well known that Cu readily oxidizes in air.⁵⁹

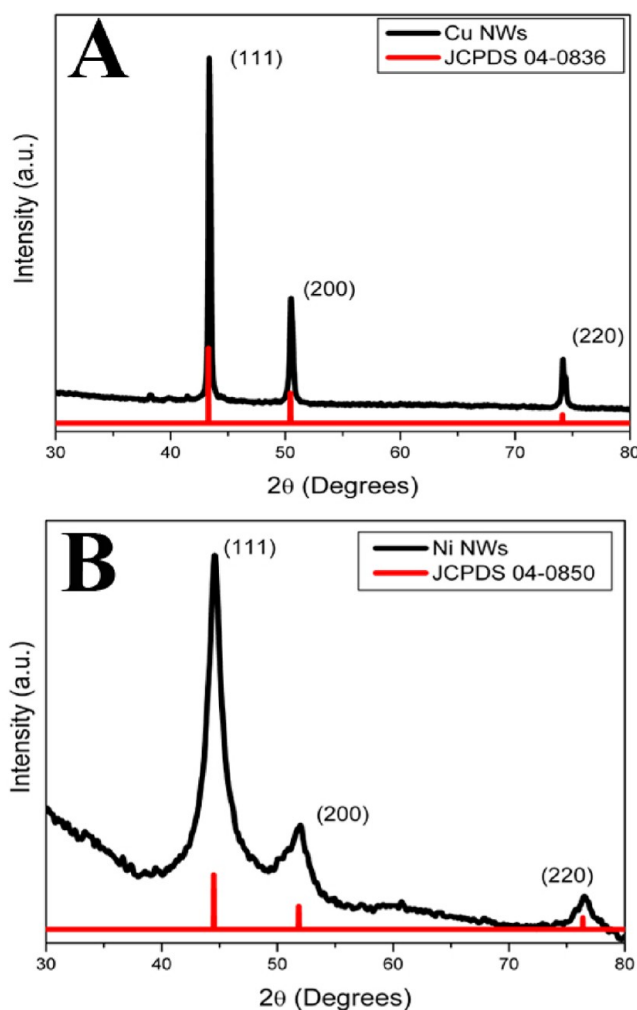


Figure 1. XRD patterns from (A) as-prepared Cu nanowires (top curve in black) and the corresponding JCPDS standard for Cu (bottom curve in red); (B) as-prepared NWs (top curve in black) and the corresponding JCPDS standard for Ni (bottom curve in red).

With respect to the Ni NWs, most diffraction peaks could be ascribed to the JCPDS #04-0850 for crystalline *fcc* Ni. We should also note that the actual amount of Ni NWs we obtained in our synthetic protocols is not as quantitatively substantial as that of Cu NWs, perhaps due to the lower diffusion rate for Ni as compared with Cu. Hence, not surprisingly, higher background peaks and lower signal-to-noise ratios were observed in Figure 1B. It is important to note that no “expected” impurity peaks, including nickel oxide, nickel hydroxide, and analogous metal oxides, were observed. Since Ni does not oxidize as easily as Cu (based on known oxidation potentials, i.e., $E^\circ = -0.34$ V and $+0.25$ V for Cu and Ni, respectively), because the oxidized form is relatively more stable for Cu, it is reasonable that these oxide peaks are not actually observed under these relatively mild reaction conditions. However, no definitive conclusion could be drawn concerning the degree of surface oxidation based solely on XRD data, since the impurity peaks might potentially have been overwhelmed by the background. We accounted for this possible problem with additional more sensitive EELS analysis.

ii. Electron Microscopy. (a). *Cu NWs.* The size and morphology of the NW samples were observed using FE-SEM, TEM, and HR-TEM. Panels A and C of Figure 2 as well as the

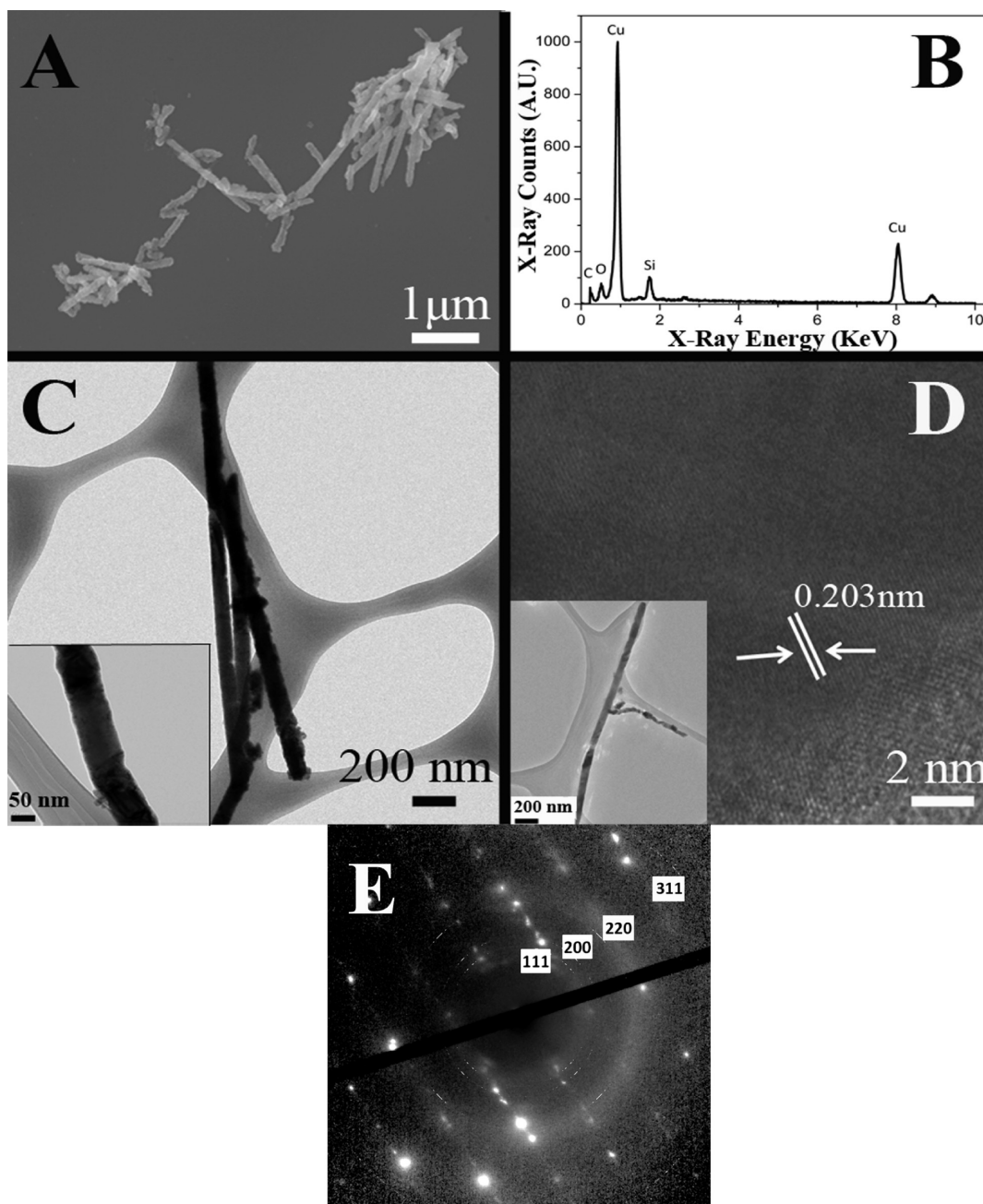


Figure 2. TEM and SEM images of isolated Cu NWs (A, C, higher magnification image as inset to (C)) prepared using template membranes possessing 50 nm pore diameters. EDS spectrum of as-prepared Cu NWs (B). The Si peak is associated with the silicon wafer. The higher magnification TEM image (D) denotes a localized area of a typical nanowire (lower resolution image in the lower left inset to (D)). Selected area electron diffraction pattern with assigned diffraction spots is shown in (E).

inset to C highlight SEM and TEM images of the Cu NWs, respectively, prepared within the pores of a 50 nm polycarbonate template membrane. These images demonstrate the presence of crystalline nanorods with a roughened surface morphology throughout their entire length with an average diameter of 100 ± 13 nm. These TEM images are representative of an overall distribution of not only dispersed but also aggregated nanowire bundles. EDS analysis (Figure 2B) suggests that we formed elemental Cu, though some degree of oxygen and carbon was also noted, an observation that may originate from either the NW sample itself, the sampling environment, or the presence of some degree of oxidation, possibly ascribed to the nanowire surface species as

well as to any residual polycarbonate template. The noticeable Si peak can be attributed to the underlying silicon wafer.

To further analyze Cu nanowires (lower left inset to Figure 2D), a single arbitrary nanowire structure was probed at the atomic scale using HR-TEM analysis. On the basis of the HR-TEM results (Figure 2D), the measured interplanar distance of 0.203 nm was consistent with the (111) plane of the *fcc* phase of crystalline Cu. Complementary SAED (Figure 2E) analysis shows that the diffraction patterns highlighting the 111, 200, 220, and 311 planes, respectively, can be indexed to crystalline Cu and are in reasonable agreement with the complementary XRD data.

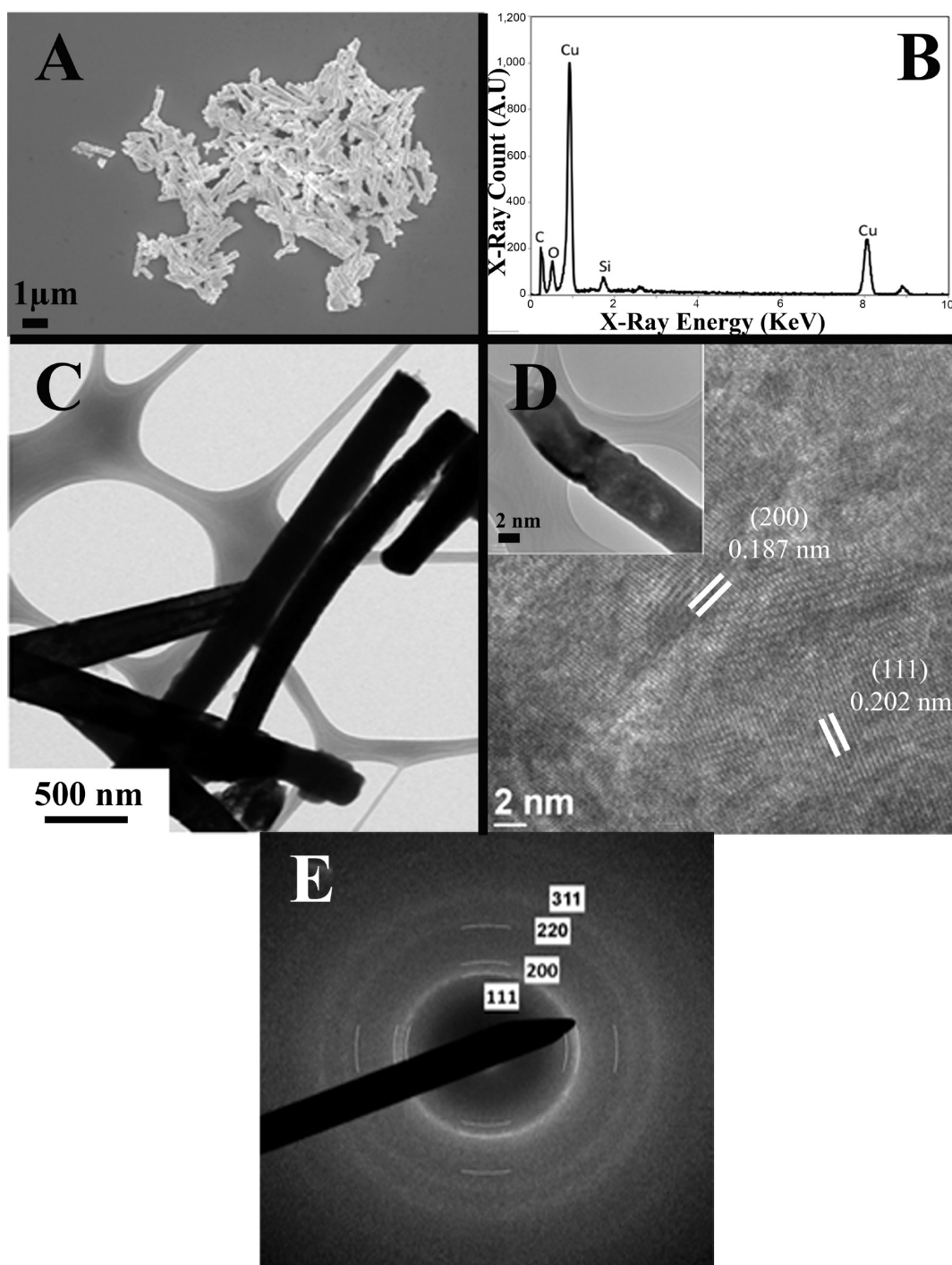


Figure 3. TEM and SEM images of isolated Cu NWs (A, C) prepared using template membranes possessing 200 nm pore diameters. EDS spectrum of as-prepared Cu NWs (B). The Si peak is associated with the silicon wafer. The TEM image (upper lefthand inset in D) denotes the region where a higher resolution image (D) was obtained. Selected area electron diffraction pattern is presented in (E).

As for the analogous Cu NWs, prepared using complementary 200 nm templates, panels A and C of Figure 3 illustrate representative SEM and TEM images of the Cu NWs. The images also demonstrate the presence of roughened NWs with an average diameter of 233 ± 19 nm and an average length of ~ 1.5 μm. On the basis of EDS analysis (Figure 3B), we note that Cu is certainly present within the sample. Peaks corresponding to carbon and oxygen can be ascribed to residual impurities arising from the template, the sampling environment, and possibly some level of oxidation. The

noticeable Si peak can be attributed to the underlying silicon wafer.

Upon the basis of the HR-TEM results (Figure 3D), the Cu NWs (upper lefthand inset to Figure 3D) were found to be polycrystalline in nature, analogous to what we have noted for other types of nanowires in prior reports under similar reaction conditions.^{47,51} Measured interplanar distances of 0.202 and 0.187 nm are consistent with the expected (111) and (200) planes, respectively. All of these data point to the formation of the *fcc* phase of crystalline Cu. Complementary SAED (Figure

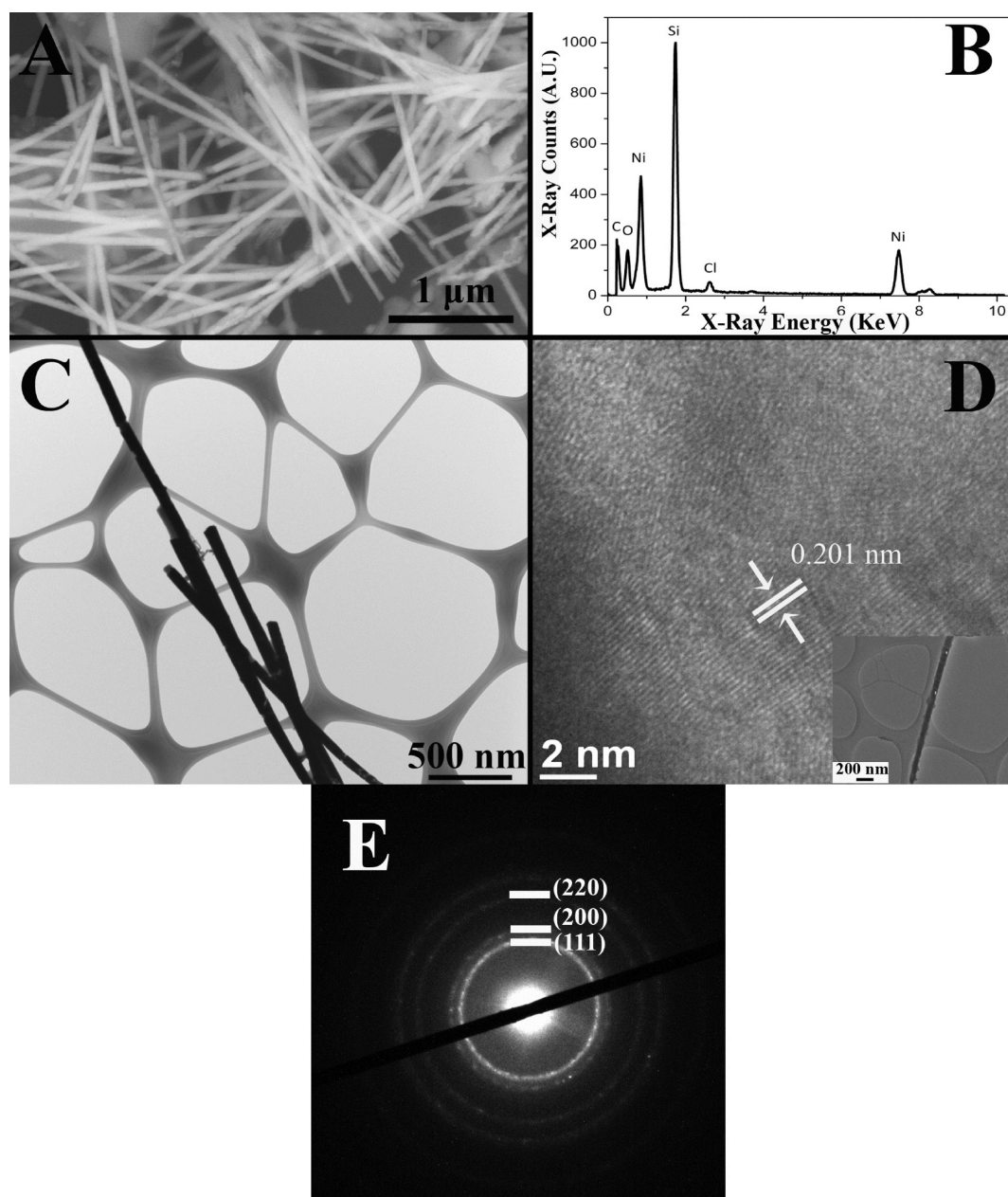


Figure 4. TEM and SEM images of as-prepared Ni NWs (A and C) prepared using template membranes possessing 50 nm pore diameters. EDS spectrum of the isolated Ni NWs (B) with the Si peak correlated with the presence of the underlying silicon wafer. The TEM image (lower right inset to D) denotes the region where the higher resolution TEM image (D) was taken as well as the SAED pattern (E).

3E) analysis shows that the diffraction patterns, possessing features associated with the 111, 200, 220, and 311 planes, respectively, can be indexed to crystalline Cu and are consistent with the complementary XRD data.

(b). *Ni NWs.* The size and morphology of the NW samples were also observed using FE-SEM, TEM, and HR-TEM analysis. Panels A and C of Figure 4 show SEM and TEM images of the Ni NWs, respectively, using a 50 nm polycarbonate template. These images are consistent with the presence of crystalline, homogeneous, and uniform nanorods throughout their entire length, possessing an average diameter of 92 ± 10 nm. The TEM images highlight both dispersed as well as aggregated nanowire bundles. The EDS analysis (Figure 4B) is indicative of the presence of elemental Ni in addition to some degree of oxygen and carbon present. The latter

contamination may likewise be ascribed to the NW sample, the sampling environment, as well as the presence of oxidation emanating from the nanowire surface and/or from the residual polycarbonate template, respectively. The presence of the silicon (Si) peak can be attributed to the silicon wafer.

To further study typical Ni nanowires (lower righthand inset to Figure 4D), an arbitrary individual structure was analyzed at the atomic scale using HR-TEM. On the basis of the HR-TEM image (Figure 4D), the observed, measured interplanar distance of 0.201 nm was consistent with the (111) plane of the *fcc* phase of the crystalline Ni observed. Complementary SAED data (Figure 4E) underscore a diffraction pattern, composed of diffuse rings, which can be indexed to the 111, 200, and 220 planes, respectively, of polycrystalline Ni, a scenario in good agreement with prior XRD results.

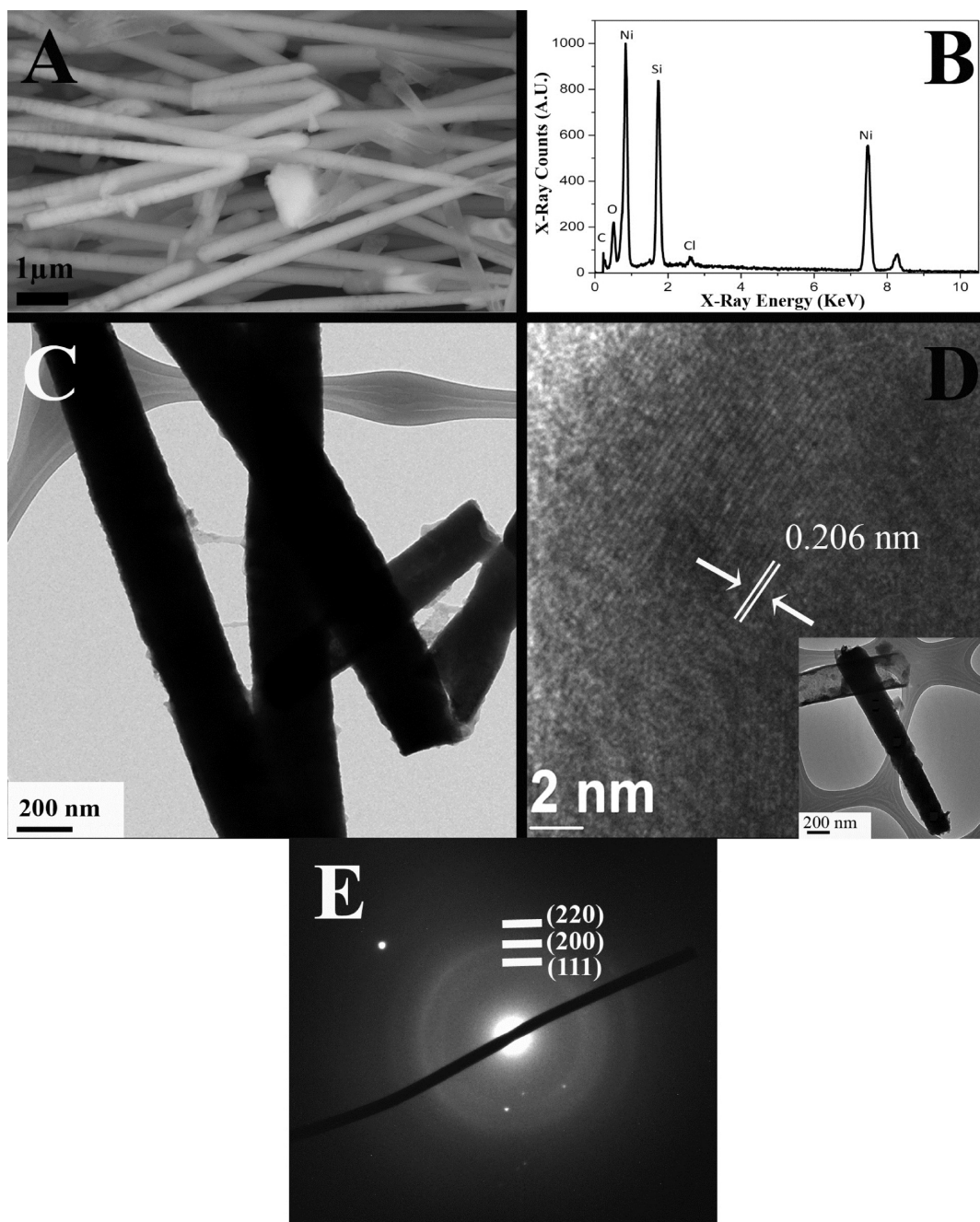


Figure 5. TEM and SEM images of as-prepared Ni NWs (A and C) prepared using template membranes possessing 200 nm pores. EDS spectrum of the isolated Ni NWs (B) with the Si peak correlated with the presence of the underlying silicon wafer. The lower magnification image (lower righthand inset to D) denotes the nanowire where the higher resolution TEM image (D) was taken as well as the SAED pattern (E).

As for the analogous Ni NWs, prepared using complementary 200 nm templates, panels A and C of Figure 5 show representative SEM and TEM images of these nanostructures. These images demonstrate the formation of smooth NWs possessing average diameters of 225 ± 33 nm with average lengths of a micrometer. We note that some of the nanowires appeared to be noticeably bent and exhibit mechanical flexibility, an observation which has been ascribed to sample processing effects. Nonetheless, prior literature has shown that at room temperature, Ni NWs are often elastic up to a threshold of 7.5% strain at different strain rates with a yield stress of 5.5 GPa,⁶⁰ a value comparable to that of Nylon ($\sim 2\text{--}4$ GPa).⁶¹ On the basis of EDS analysis (Figure 5B), we note that

Ni is present within the sample. Peaks corresponding to carbon and oxygen likely can be ascribed to factors associated with the presence of residual template, an impure sampling environment, and possible oxidation effects. The apparent Si peak can be attributed to the underlying silicon wafer.

The NWs were also further probed at higher resolution. Specifically, based on HR-TEM results (Figure 5D), the Ni NWs (lower right inset to Figure 5D) were found to be crystalline in nature with a measured interplanar distance of 0.206 nm, data which are consistent with the presence of the (111) plane, corresponding to the *fcc* phase of crystalline Ni. Complementary SAED (Figure 5E) analysis suggests that the diffraction patterns associated with the 111, 200, and 220

planes, respectively, can be ascribed to crystalline Ni, and our results are also in reasonable agreement with the complementary XRD data.

iii. UV–visible Spectroscopy. Panels A and B of Figure 6 features UV–visible spectra of Cu and Ni NWs produced under

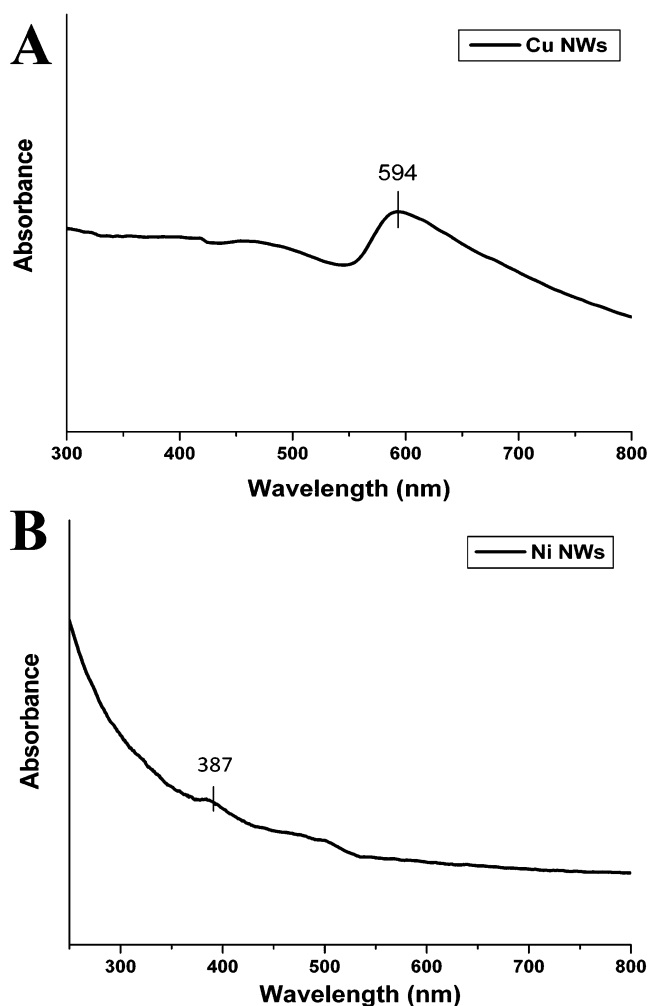


Figure 6. UV–visible absorption spectra of Cu NWs (A) and Ni NWs (B).

ambient conditions. The absorption spectrum for Cu highlights a surface plasmon peak centered at ~ 594 nm, which is somewhat red-shifted from what has been previously shown in the literature, but this observation may possibly be due to an increase in diameter and aspect ratio as well as to a higher degree of aggregation by comparison with conventional Cu nanoparticles previously studied.^{62–66} The absence of a peak near 370 nm, normally ascribed to Cu_2O , indicates that there is no observable sign of widespread sample oxidation, although we cannot rule out the presence of localized oxidation upon air exposure, evident from the XRD data. Figure 6B highlights the presence of UV–visible absorption spectra of Ni NWs with an absorbance peak of ~ 387 nm, which is in good agreement with the literature.^{38,67}

iv. Electron Energy Loss Spectroscopy (EELS) Cross Sectional Analysis. Cross-sectional line scans were collected on selected metal NWs in order to observe the thickness of the oxide layers on these nanomaterials. It is evident that we form a primary central “core” of elemental Cu and Ni NWs, respectively, with a very thin outer oxide “shell”. For the Cu NWs, based on spatially resolved EELS spectra (Figure 7A,B), it is apparent that the nanostructure surface has circumferentially oxidized with a thin outer oxide layer possessing a thickness of ~ 30 nm (based on full width at half-maximum measurements, fwhm). This observation may be due in part to exposure to air during processes associated with characterization, such as sample preparation and image acquisition. As for the Ni NWs, based on spatially resolved EELS spectra (Figure 8A,B), the corresponding thin outer oxide layer appears to be roughly ~ 20 nm in thickness, based on fwhm measurements, as evidenced by the magnitude and spatial breadth of the elemental oxygen signal on the nanowire perimeter. The intensity and uniformity of the Ni peak are consistent with a reasonably homogeneous elemental Ni nanostructure as a result of the room-temperature synthesis process. In effect, the oxygen peak distribution is strongest at the circumferential edges, consistent with the formation of a narrow outer surface oxide layer, measuring between 20 and 30 nm. Moreover, the oxygen signal diminishes in intensity within the interior of the wire structure itself.

v. Photocatalytic Degradation Results. (a). *Cu NWs.* In Figure 9A, C_0 represents the initial concentration of MO, and C denotes the time-dependent concentration, reflecting a time-

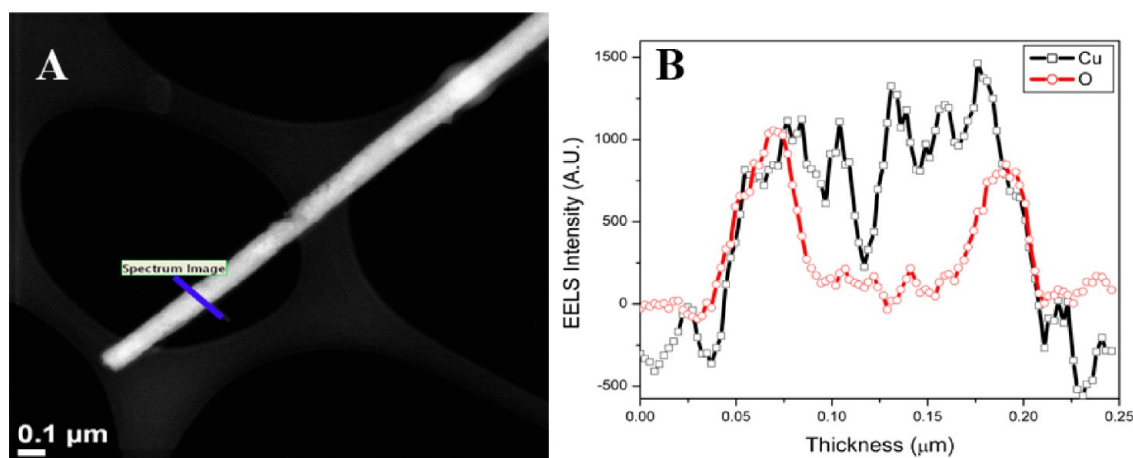


Figure 7. Electron energy loss spectroscopy (EELS) cross-sectional analysis of an as-prepared copper nanowire. Signal intensities for copper and oxygen (B) correspond to the blue slice in the survey image, highlighted in (A).

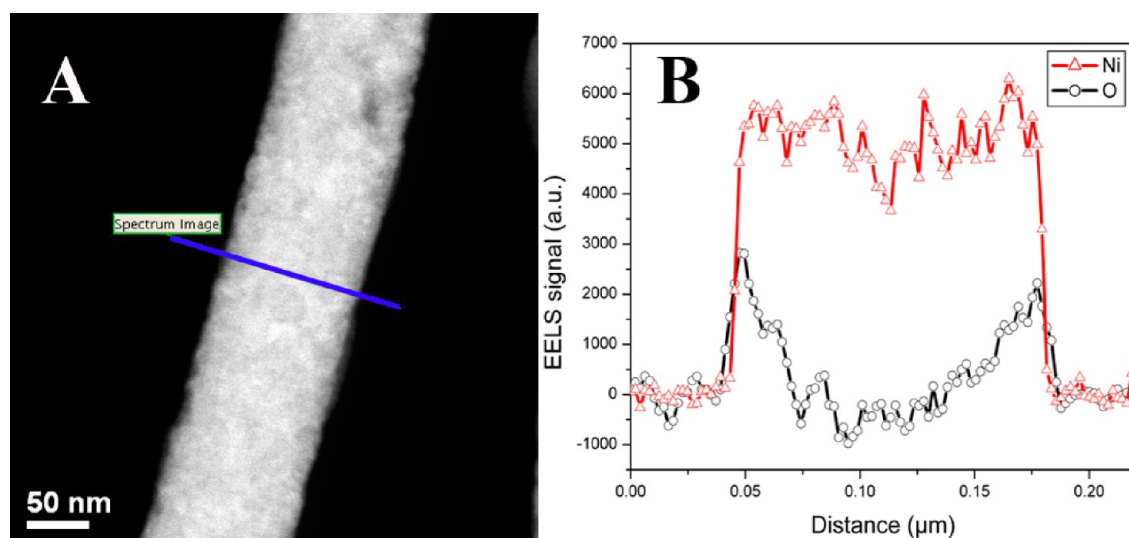


Figure 8. Electron energy loss spectroscopy (EELS) cross-sectional analysis of an as-prepared nickel nanowire. Signal intensities for nickel and oxygen (B) correspond to the blue slice in the survey image highlighted in (A).

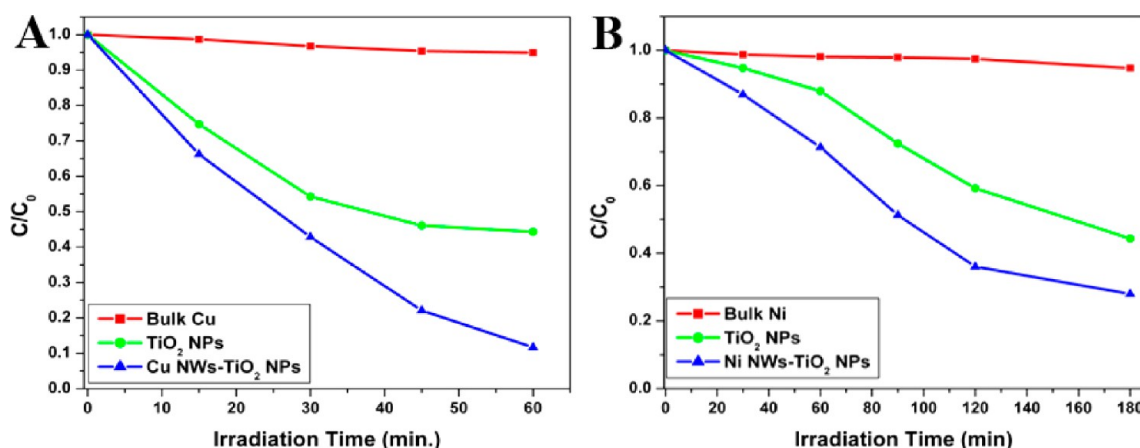


Figure 9. Photocatalytic activities of composites of (A) TiO_2 coupled with Cu NWs for the degradation of Methyl Orange as well as of (B) TiO_2 coupled with Ni NWs for Methylene Blue degradation. Analogous, comparative photodegradation data with control samples consisting of (i) bulk metal (i.e., Cu and Ni) and (ii) TiO_2 NPs are also shown.

dependent decoloration in this case, of MO, after UV irradiation. Under UV irradiation illumination ($\lambda_{\text{ex}} = 366$ nm (3.4 eV)), electrons are excited from a filled valence band to an empty conduction band, thereby generating electron–hole pairs in wide band gap (i.e., 3.2 eV) TiO_2 NPs. Hence, photodegradation occurs⁶⁸ as a result of the interaction of dye molecules with reactive oxidizing species generated on the nanoparticulate metal oxide surface when either (i) the holes react with adsorbed OH^- to produce hydroxyl radicals or (ii) electrons combine with adsorbed electron acceptors such as oxygen to create O_2^- , for instance.⁶⁹ Not surprisingly, our TiO_2 NPs showed a $\sim 50\%$ reduction in MO dye absorption after 1 h of reaction.

By contrast, the composite containing Cu NWs coupled with TiO_2 gave rise to a sizable $\sim 90\%$ decrease in the absorption level of MO, after an hour of reaction. This observation may have potentially been due to a number of reasons. First, because the surface potential of Cu- TiO_2 composites is much less than that of pure TiO_2 during UV illumination, the composite surface possesses abundant electronic traps (such as oxygen vacancies and Cu^{2+} species), which can intrinsically decrease

the recombination rate of photoinduced charge carriers including electron–hole pairs,^{70,71} thereby leading to enhanced photocatalytic efficiency.^{72,73} Second, the interfacial charge transfer from the photoexcited TiO_2 to the proximal, coupled Cu generates reactive radical species such as $\cdot\text{OH}$.^{55,74} Third, Cu^{2+} may reduce to Cu^+ in the presence of a photogenerated electron, which can subsequently react with H_2O_2 to create larger quantities of reactive and ultimately destructive surface radical species, including primarily $\cdot\text{OH}$, all of which are ultimately responsible for the high oxidant activity that results in the organic dye compound degradation in these photocatalytic reactions.^{70,71,74,75} Fourth, the composite provides for a moderate specific surface area for more abundant reaction sites as compared with their elemental analogues.⁵⁶ By contrast, bulk Cu exhibited relatively poor performance for the degradation of MO, approximately after an hour of reaction activity.

(b). *Ni NWs.* In Figure 9B, C_0 denotes the initial concentration of MB, and C is the corresponding time-dependent concentration, manifested as a signal decrease associated with the decoloration of MB under ambient

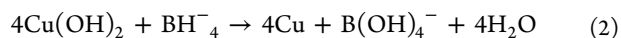
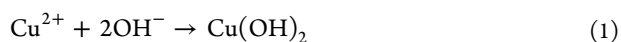
fluorescent white light exposure. Upon the basis of the photodegradation results (Figure 9B), TiO₂ NPs showed a ~50% reduction in MB absorption after 3 h of reaction. This result is consistent with previous literature, as TiO₂ is photoactive in the UV region.^{58,69,76} By comparison, use of the corresponding composites composed of Ni NWs associated with TiO₂ led to a greater than 60% decrease in the absorption value of MB over 3 h as compared with bulk Ni.

This observed increased degradation activity is likely caused by the enhanced activity of more readily produced photo-generated electrons and corresponding hole pairs, a process which occurs relatively more quickly based on the reduced band gap of the Ni-TiO₂ composite (2.28 eV)⁵⁸ as compared with bare, undoped TiO₂ (3.2 eV)⁵⁸ with the decrease in bandgap for the composite attributable to the “electron acceptor” character of Ni. These photogenerated electrons can either assist in the reduction of the MB dye directly or react with either O₂, OH[−], or H₂O to generate radicals (such as O₂^{•−}) that are known to be powerful oxidizing agents.⁷⁷ We should note that, based on existing literature, when Ni NPs were incorporated with TiO₂, photodegradation results of ~50% were recorded; these data are comparable to what we have observed herein.

We also find that the photodegradation ability of TiO₂ with respect to MO is relatively greater than and exhibits different kinetic behavior as compared with TiO₂ in the presence of MB (i.e., blue curves in Figure 9, panels A and B, respectively). That experimental observation can mainly be attributed to differential adsorption capacities of MO and MB onto the surfaces of TiO₂ NPs.⁷⁶ Specifically, because there are likely more positively charged sites as opposed to negatively charged ones on the TiO₂ surface, MO, which is an anionic dye, will preferentially and more efficiently adsorb onto the TiO₂ surface through the mediation of favorable electrostatic interactions as compared with MB, which is a cationic dye. The result therefore is a more effective photocatalytic reaction of TiO₂ NPs with MO as compared with MB.

Nonetheless, both reactions (i.e., for Cu and Ni-incorporated TiO₂ composites) were calculated to be first-order reactions, following the $\ln(C_0/C)$ vs irradiation time plots (Figure S9, panels A and B, respectively), from whence we were able to derive associated reaction rate constants (Table S3, Supporting Information). Indeed, the rate constants were computed to be $3.6 \times 10^{-2} \text{ min}^{-1}$ for Cu NW-TiO₂ and $7.7 \times 10^{-3} \text{ min}^{-1}$ Ni NW-TiO₂ heterostructures, respectively, suggestive of a faster degradation potential as compared with either bare TiO₂ NPs or analogous heterostructures (i.e., $4.2 \times 10^{-3} \text{ min}^{-1}$ for Cu-TiO₂ composites) previously reported.⁵⁶

vi. Plausible Growth Mechanism. Cu. We note that the role of the NaOH is to adjust the pH as well as to enhance the reduction process in water.^{9,10} Consequently, we expect that the NW growth can be rationalized in terms of redox reactions, given in eqs 1 and 2 under basic conditions at room temperature.⁷⁸

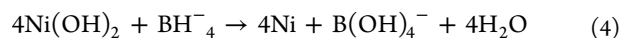
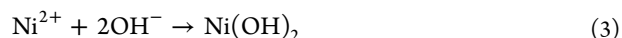


Additional experiments were conducted under acidic conditions. In a typical example, 50 mM of HCl solution was prepared separately in water and then added to the NaBH₄ solution (in water) in one side arm with 50 mM CuCl₂ precursor solution on the other half cell of the U-tube. HCl

was used, because it is known to enhance the hydride generation associated with NaBH₄, and as a result, may help to increase the rate of the reaction.⁷⁹ Nanowire growth did in fact take place. However, a substantial cuprous oxide impurity layer (Cu₂O) was noted via HRTEM, XRD, and UV–visible analysis (Figure S3A–D, Supporting Information). As a result, a second reduction step had to be incorporated in order to generate elemental Cu NWs, and that additional reduction purification process unfortunately yielded highly fragmented nanowires (lower left inset of Figure S4B, Supporting Information).⁸⁰

Other reducing agents have also been tried. Examples included hydrazine (N₂H₄, $E^\circ = -0.33 \text{ V}$) and dimethylamine borane ((CH₃)₂NH·BH₃, DMAB). In a typical reaction, N₂H₄ and CuCl₂ solutions were added simultaneously. Instantaneously, the solutions turned cloudy, and then, a darker hued impurity started to form. As a result, the reaction was stopped, the template was removed, and it was found that the hydrazine had been dissolving the template itself, thereby forming black copper particles, whereas the creamy residue likely represented the remnant template (Figure S5, Supporting Information). Regarding DMAB, its reducing solution seemed to migrate and diffuse through the template pores slightly faster than the corresponding CuCl₂ solution. This observation indicated that the local DMAB concentration was likely reduced to be less than 50 mM, which might conceivably have lowered the nanowire yield as a result. Not surprisingly, no crystalline nanowires were produced with DMAB. From our study of the use of different reducing agents, we noted that NaBH₄ is an excellent reducing agent of choice for our template-based coprecipitation method under ambient conditions.

Ni. In the context of reactions using templates possessing 50 nm pore sizes, with the reducing agent concentration set at a relatively constant concentration of 0.05 M, nickel precursor concentrations of 0.025 and 0.05 M produced no Ni NWs, presumably due to a lack of a sufficient probability of necessary nucleation events within the template pores within a set time period. As a result, slightly higher, i.e., 0.075 and 0.1 M, Ni concentrations were used and did in fact produce uniform, ~50 nm diameter wires (Figure 4). A reasonable reaction mechanism to explain our observations is described as follows, in eqs 3 and 4, under basic conditions:



As for reactions within the larger 200 nm diameter template pores giving rise to ~200 nm diameter wires (Figure 5), the previously mentioned Ni concentrations (i.e., 0.075 M (Figure S7, Supporting Information) and 0.1 M, respectively) were also tested, but these reaction conditions yielded either hollow nanotubes or essentially nothing of interest, i.e., no nanowires. As a result, the NaBH₄ concentration was maintained at 0.05 M, while the metal precursor concentration was systematically varied from 0.025 to 0.1 M. We noted that as the reducing agent concentration was increased from 0.025 M (Figure S8, Supporting Information) to 0.05 M, uniform filled wires were more likely to form. This observation may possibly be due to increasingly favorable intramolecular interactions between reagent molecules (i.e., homogeneous nucleation) versus less favorable intermolecular interactions with the pore walls (i.e., heterogeneous nucleation), as the reducing agent concentration increases.⁴⁷ However, as the reducing agent concentration was

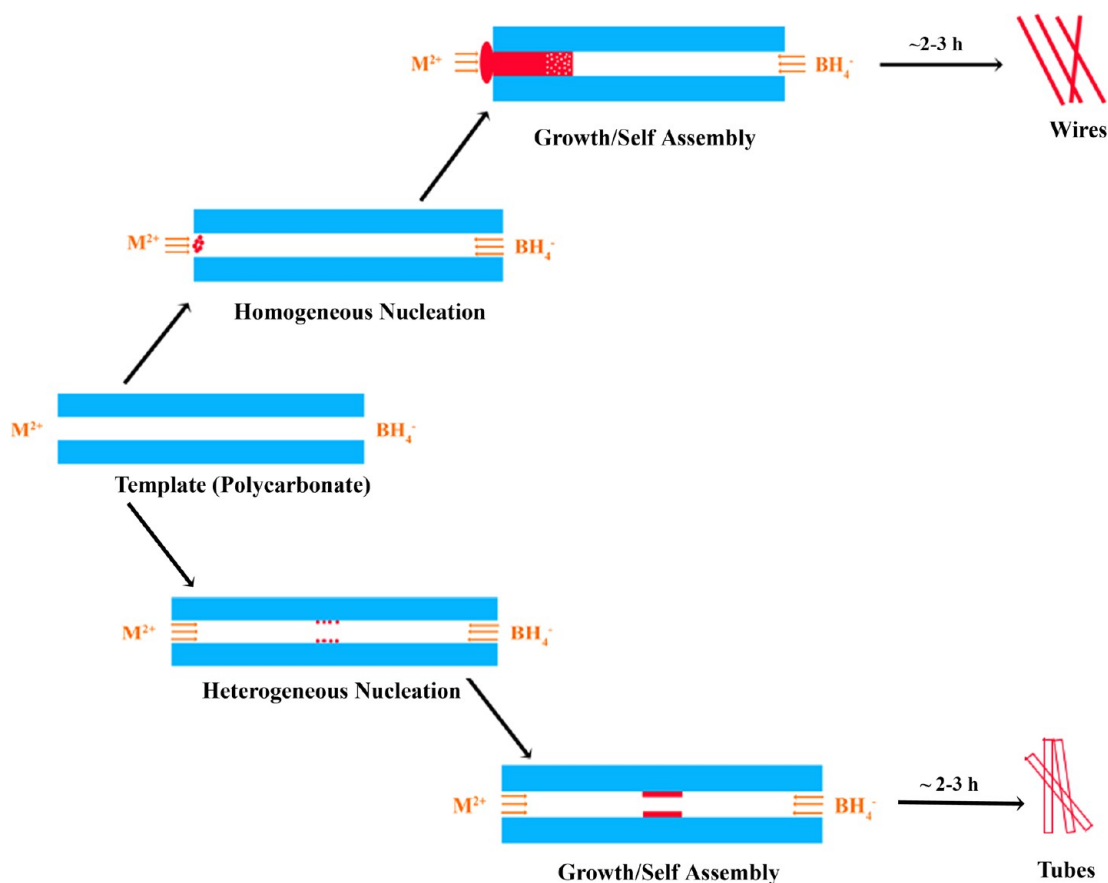


Figure 10. Plausible growth mechanism for Cu and Ni nanowires (NWs) and nanotubes (NTs) under room temperature conditions.

increased even further (i.e., 0.075 and 0.1 M), no wires were produced in these larger sized template membranes, suggesting a narrow parameter window for reaction optimization.

Plausible growth mechanisms for the metal nanowires and nanotubes are shown in Figure 10. Upon the basis of our previous work,⁵⁰ we believe that the growth of the NWs within the PC templates follows a two-step process. In the *first step*, the precursor and the reducing agent diffuse into the pore space and inevitably, the diffusion fronts intersect, resulting in the reduction of the metallic precursor and formation of metal seed nuclei. This initial rapid reduction followed by a nucleation process yields both a short polycrystalline NW segment within the template pore and a thin layer of metallic material on the outer surfaces of the template within the reducing agent half-cell. In fact, the formation of the metallic layer on the surface of the template facing toward and thereby exposed to the reducing agent half-cell can be observed visually within the initial stages of the reaction. In the case of Cu, we noted a red color, whereas for Ni, it was black. In the *second step*, these isolated, disparate nucleation sites grow by extension throughout the porous template network. In a homogeneous nucleation scenario, as-formed metal nuclei preferentially self-assemble with each other into either filled wire-like or rod-like motifs, whereas in the analogous heterogeneous nucleation scenario, preferred confinement of growth along the pore walls themselves can therefore lead to the generation of primarily hollow tube-like motifs upon the elongation and self-assembly of the as-formed nuclei.

CONCLUSIONS

Our laboratory has reported on a reliable, reproducible, and seedless growth under ambient conditions using a solution-based template methodology of difficult-to-isolate, crystalline, homogeneous elemental Cu and Ni nanowires with a plausible growth mechanism proposed. The porous polycarbonate templates we have used have enabled us not only to control size but also to direct nanowire growth and morphology within the membrane channels. These nanowires have been extensively characterized using complementary optical spectroscopy, electron microscopy, as well as diffraction techniques. Moreover, the degree of oxidation of these nanowires was probed both qualitatively and quantitatively using both EDS and EELS.

An enhanced photocatalytic activity of metallic Cu and Ni nanowires (deliberately coupled with TiO₂) was observed as compared with both bulk and commercial TiO₂ nanoparticulate control samples in the presence of two different and distinctive dyes, namely, MO and MB, respectively. Both Cu-TiO₂ and Ni-TiO₂ composites, incorporating metallic NWs, gave rise to first order rate reactions for their respective dyes, implying comparable behavior with what had been previously observed in the literature. Overall, these functional improvements in performance could be primarily ascribed to active surface area and electronic enhancement effects associated with the composites as compared with TiO₂ itself.

■ ASSOCIATED CONTENT

■ Supporting Information

For as-prepared Cu nanowires, Table S1 summarizes all experimental runs; Figures S1–S4 include electron microscopy images as well as diffraction and spectroscopy data; and Figures S5 and S6 are optical images of experimental observations. For as-prepared Ni nanowires, Table S2 summarizes all experimental runs; Figures S7 and S8 include electron microscopy images and EDS analyses. Figure S9 and Table S3 highlight the photocatalytic behavior of Cu/Ni NW-TiO₂ composites in the presence of organic dyes. This material is available free of charge via the Internet at <http://pubs.acs.org/>.

■ AUTHOR INFORMATION

Corresponding Author

*E-mail: stanislaus.wong@stonybrook.edu; sswong@bnl.gov.

Notes

The authors declare no competing financial interest.

■ ACKNOWLEDGMENTS

Research (including support for all authors) was provided by the U.S. Department of Energy, Basic Energy Sciences, Materials Sciences and Engineering Division. Certain experiments in this manuscript, such as TEM and EELS, were performed in part at the Center for Functional Nanomaterials, located at Brookhaven National Laboratory, which is supported by the U.S. Department of Energy under Contract No. DE-AC02-98CH10886.

■ REFERENCES

- (1) Feldheim, D. L.; Foss, C. A. *Metal Nanoparticles: Synthesis, Characterization, and Applications*; Marcel Dekker, Inc: New York, 2002; pp 8–9.
- (2) Maiera, S. A.; Atwater, H. A. Plasmonics: Localization and guiding of electromagnetic energy in metal/dielectric structures. *J. Appl. Phys.* **2005**, *98* (1), 011101–1–011101–10.
- (3) Siow, K. S.; Tay, A. A. O.; Oruganti, P. Mechanical properties of nanocrystalline copper and nickel. *Mater. Sci. Technol.* **2004**, *20* (3), 285–294.
- (4) Sanders, P. G.; Youngdahl, C. J.; Weertman, J. R. The strength of nanocrystalline metals with and without flaws. *Mater. Sci. Eng.* **1997**, *234–236*, 77–82.
- (5) Rao, C. N. R.; Kulkarni, G. U.; Govindaraj, A.; Satishkumar, B. C.; Thomas, P. J. Metal nanoparticles, nanowires, and carbon nanotubes. *Pure Appl. Chem.* **2000**, *72* (1–2), 21–33.
- (6) Kleiman, G. G.; Landers, R.; de Castro, S. G. C. Core hole screening and electronic structure information. *J. Electron Spectrosc. Relat. Phenom.* **1995**, *72*, 199–203.
- (7) Zhou, Z.-Y.; Tian, N.; Li, J.-T.; Broadwell, I.; Sun, S.-G. Nanomaterials of high surface energy with exceptional properties in catalysis and energy storage. *Chem. Soc. Rev.* **2011**, *40* (7), 4167–4185.
- (8) Bruce, P. G.; Scrosati, B.; Tarascon, J.-M. Nanomaterials for Rechargeable Lithium Batteries. *Angew. Chem. Int. Ed.* **2008**, *47* (16), 2930–2946.
- (9) Dang, T. M. D.; Le, T. T. T.; Fribourg-Blanc, E.; Dang, M. C. Synthesis and optical properties of copper nanoparticles prepared by a chemical reduction method. *Adv. Nat. Sci.: Nanosci. Nanotechnol.* **2011**, *2* (1), 150091–150096.
- (10) Wang, Y.; Biradar, A. V.; Wang, G.; Sharma, K. K.; Duncan, C.; Rangan, S.; Asefa, T. Controlled Synthesis of Water-Dispersible Faceted Crystalline Copper Nanoparticles and Their Catalytic Properties. *Chem.—Eur. J.* **2010**, *16* (35), 10735–10743.
- (11) Rathmell, A. R.; Bergin, S. M.; Hua, Y.-L.; Li, Z.-Y.; Wiley, B. J. The Growth Mechanism of Copper Nanowires and Their Properties in Flexible, Transparent Conducting Films. *Adv. Mater.* **2010**, *22* (32), 3558–3563.
- (12) Wu, H.; Kong, D.; Ruan, Z.; Hsu, P.-C.; Wang, S.; Yu, Z.; Carney, T. J.; Hu, L. F.; an, S.; Cui, Y. A transparent electrode based on a metal nanotrough network. *Nat. Nanotechnol.* **2013**, *8* (6), 421–425.
- (13) Zhao, Y.; Zhang, Y.; Li, Y.; He, Z.; Yan, Z. Rapid and large-scale synthesis of Cu nanowires via a continuous flow solvothermal process and its application in dye-sensitized solar cells (DSSCs). *RSC Adv.* **2012**, *2*, 11544–11551.
- (14) Kang, M.-G.; Park, H. J.; Ahn, S. H.; Guo, L. J. Transparent Cu nanowire mesh electrode on flexible substrates fabricated by transfer printing and its application in organic solar cells. *Sol. Energy Mater. Sol. Cells* **2010**, *94*, 1179–1184.
- (15) Ye, S.; Rathmell, A. R.; Stewart, I. E.; Ha, Y.-C.; Wilson, A. R.; Chen, Z.; Wiley, B. J. A rapid synthesis of high aspect ratio copper nanowires for high-performance transparent conducting films. *Chemical Communications* **2014**, *50*, 2562–2564.
- (16) Lupan, O.; Pauporte, T.; Viana, B.; Aschehoug, P. Electrodeposition of Cu-doped ZnO nanowire arrays and heterojunction formation with p-GaN for color tunable light emitting diode applications. *Electrochim. Acta* **2011**, *56*, 10543–10549.
- (17) Halaciuga, I.; LaPlante, S.; Goia, D. Method for preparing dispersed crystalline copper particles for electronic applications. *Rapid Commun.* **2009**, *24* (10), 3237–3240.
- (18) Zhao, Y.; Zhang, Y.; Li, Y.; He, Z.; Yan, Z. Rapid and large-scale synthesis of Cu nanowires via a continuous flow solvothermal process and its application in dye-sensitized solar cells. *RSC Adv.* **2012**, *2* (30), 11544–11551.
- (19) Cempel, M.; Nikel, G. Nickel: A Review of Its Sources and Environmental Toxicology. *Pol. J. Environ. Stud.* **2006**, *15* (3), 375–382.
- (20) Sapkal, S. B.; Shelke, K. F.; Shingate, B. B.; Shingare, M. S. Nickel Nanoparticles: An Ecofriendly and Reusable Catalyst for the Synthesis of 3,4-Dihydropyrimidine-2(1H)-ones via Biginelli Reaction. *Bull. Korean Chem. Soc.* **2010**, *31* (2), 351–354.
- (21) Ai, D.; Kang, S. Synthesis of Ni Nanopowders Using an EHA System. *Mater. Trans.* **2006**, *47* (8), 1056–1059.
- (22) Shukla, A. K.; Venugopalan, S.; Hariprakash, B. Nickel-based rechargeable batteries. *J. Power Sources* **2001**, *100* (1–2), 125–148.
- (23) Pokropivny, V.; Lohmus, R.; Hussainova, I.; Pokropivny, A.; Vlassov, S. *Introduction to Nanomaterials and Nanotechnology*; Tartu University Press: Ukraine, 2007.
- (24) Hasegawa, K.; Ohnishi, M.; Oshitani, M.; Takeshima, K.; Matsumaru, Y.; Tamura, K. Nickel — Metal Hydride Battery. *Z. Phys. Chem.* **1994**, *183*, 325–331.
- (25) Ou, M. N.; Yang, T. J.; Harutyunyan, S. R.; Chen, Y. Y.; Chen, C. D. Electrical and thermal transport in single nickel nanowire. *Appl. Phys. Lett.* **2008**, *92*, 63101–63104.
- (26) Liang, H.-W.; Liu, J.-W.; Qian, H.-S.; Yu, S.-H. Multiplex Templating Process in One-Dimensional Nanoscale: Controllable Synthesis, Macroscopic Assemblies, and Applications. *Acc. Chem. Res.* **2013**, *46* (7), 1450–1461.
- (27) Chen, Q.-c. Hydrothermal conditions for fabrication of Cu nanorods and nanowires through reduction. *Jingxi Huagong* **2005**, *22*, 417–419.
- (28) Khalil, A.; Hashaikeh, R.; Jouiad, M. Synthesis and morphology analysis of electrospun copper nanowire. *J. Mater. Sci.* **2014**, *49*, 3052–3065.
- (29) Wang, X.-h.; Chen, G.; Li, C.-y.; Yang, L.; Cao, H.; Zhou, W.-m. AC electrochemical deposition of Cu nanowire arrays and its mechanism. *Cailiao Gongcheng* **2010**, *20*–23.
- (30) Sun, X.; Xu, F. Controlling aspect ratio of copper group nanowire arrays by electrochemical deposition in the nanopores of AAO. *Adv. Mater. Res.* **2011**, *335–336*, 429–432.
- (31) Liu, X.; She, X.; Song, G.; Sun, X.; Wang, S. Preparation of patterned Cu nanowire arrays by UV-photolithography. *Dianzi Yuanjian Yu Cailiao* **2008**, *27*, 51–53.

- (32) Qingming, L.; Debi, Z.; Yamamoto, Y.; Ichino, R.; Okido, M. Preparation of Cu nanoparticles with NaBH_4 by aqueous reduction method. *Trans. Nonferrous Met. Soc. China* **2012**, *22*, 117–123.
- (33) Choi, H.; Park, S.-H. Seedless growth of free-standing copper nanowires by chemical vapor deposition. *J. Am. Chem. Soc.* **2004**, *126*, 6248–6249.
- (34) Yue, G.; Xu, Q.; Meng, G.; He, X.; Han, F.; Zhang, L. Electrochemical synthesis and magnetic properties of single-crystal and netlike poly-crystal Ni nanowire arrays. *J. Alloys Compd.* **2009**, *477* (1–2), L30–L34.
- (35) Surmawar, N. V.; Thakare, S. R.; Khaty, N. T. One-Pot, Single Step Green Synthesis of Copper Nanoparticles: SPR Nanoparticles. *Int. J. Green Nanotechnol.* **2011**, *3* (4), 302–308.
- (36) Li, X.; Wang, Y.; Song, G.; She, X.; Peng, Z.; Wang, S.; Li, J. Fabrication of highly-ordered nanopatterned copper nanowire arrays by photolithography. *J. Nanosci. Nanotechnol.* **2010**, *10*, 4363–4367.
- (37) Liu, Y.-Q.; Zheng, M.; Wang, F.-X.; Pan, G.-B. Facile microwave-assisted synthesis of uniform single-crystal copper nanowires with excellent electrical conductivity. **2012**, *2*, 11235–11237.
- (38) Guo, X.; Zheng, F.; Guo, M.; Zhang, M.; Chou, K.-C. Preparation and UV property of size-controlled monodisperse nickel nanoparticles (<10 nm) by reductive method. *Rare Met. (Beijing, China)* **2013**, *32* (2), 179–185.
- (39) Zhao, Y.; Zhang, Y.; Li, Y.; Yan, Z. Soft synthesis of single-crystal copper nanowires of various scales. *New J. Chem.* **2012**, *36*, 130–138.
- (40) Roy, A.; Srinivas, V.; Ram, S.; De Toro, J. A.; Mizutani, U. Structure and magnetic properties of oxygen-stabilized tetragonal Ni nanoparticles prepared by borohydride reduction method. *Phys. Rev. B* **2005**, *71* (18), 188443–(1–10).
- (41) Knecht, M. R.; Garcia-Martinez, J. C.; Crooks, R. M. Synthesis, Characterization, and Magnetic Properties of Dendrimer-Encapsulated Nickel Nanoparticles Containing <150 Atoms. *Chem. Mater.* **2006**, *18*, 5039–5044.
- (42) Chang, Y.; Lye, M. L.; Zeng, H. C. Large-Scale Synthesis of High-Quality Ultralong Copper Nanowires. *Langmuir* **2005**, *21* (9), 3746–3748.
- (43) Rathmell, A. R.; Wiley, B. J. The Synthesis and Coating of Long, Thin Copper Nanowires to Make Flexible, Transparent Conducting Films on Plastic Substrates. *Adv. Mater.* **2011**, *23* (41), 4798–4803.
- (44) Zhang, D.; Wang, R.; Wen, M.; Weng, D.; Cui, X.; Sun, J.; Li, H.; Lu, Y. Synthesis of Ultralong Copper Nanowires for High-Performance Transparent Electrodes. *J. Am. Chem. Soc.* **2012**, *134* (35), 14283–14286.
- (45) Krishnadas, K. R.; Sajanlal, P. R.; Pradeep, T. Pristine and Hybrid Nickel Nanowires: Template-, Magnetic Field-, and Surfactant-Free Wet Chemical Synthesis and Raman Studies. *J. Phys. Chem. C* **2011**, *115* (11), 4483–4490.
- (46) Zhang, F.; Yiu, Y.; Aronson, M.; Wong, S. S. Exploring the Room-Temperature Synthesis and Properties of Multifunctional Doped Tungstate Nanorods. *J. Phys. Chem. C* **2008**, *38*, 14816–14824.
- (47) Zhou, H.; Wong, S. S. A Facile and Mild Synthesis of 1-D ZnO , CuO , and $\alpha\text{-Fe}_2\text{O}_3$ Nanostructures and Nanostructured Arrays. *ACS Nano* **2008**, *2* (5), 944–958.
- (48) Koenigsmann, C.; Sutter, E.; Chiesa, T. A.; Adzic, R. R.; Wong, S. S. Highly Enhanced Electrocatalytic Oxygen Reduction Performance Observed in Bimetallic Palladium-Based Nanowires Prepared under Ambient, Surfactantless Conditions. *Nano Lett.* **2012**, *12* (4), 2013–2020.
- (49) Koenigsmann, C.; Tan, Z.; Peng, H.; Sutter, E.; Jacobskind, J.; Wong, S. S. Multifunctional Nanochemistry: Ambient, Electroless, Template-Based Synthesis and Characterization of Segmented Bimetallic Pd/Au and Pd/Pt Nanowires as High-Performance Electrocatalysts and Nanomotors. *Isr. J. Chem.* **2012**, *52* (11–12), 1090–1103.
- (50) Koenigsmann, C.; Santulli, A. C.; Sutter, E.; Wong, S. S. Ambient Surfactantless Synthesis, Growth Mechanism, and Size-Dependent Electrocatalytic Behavior of High-Quality, Single Crystalline Palladium Nanowires. *ACS Nano* **2011**, *5* (9), 7471–7487.
- (51) Zhang, F.; Wong, S. S. Controlled Synthesis of Semiconducting Metal Sulfide Nanowires. *Chem. Mater.* **2009**, *21* (19), 4541–4554.
- (52) Zhang, F.; Wong, S. S. Ambient large-scale template-mediated synthesis of high-aspect ratio single-crystalline, chemically doped rare-earth phosphate nanowires for bioimaging. *ACS Nano* **2010**, *4* (1), 99–112.
- (53) Mao, Y.; Zhang, F.; Wong, S. S. Ambient Template-Directed Synthesis of Single-Crystalline Alkaline-Earth Metal Fluoride Nanowires. *Adv. Mater.* **2006**, *18* (14), 1895–1899.
- (54) Zhou, H.; Zhou, W.-p.; Adzic, R. R.; Wong, S. S. Enhanced Electrocatalytic Performance of One-Dimensional Metal Nanowires and Arrays Generated via an Ambient, Surfactantless Synthesis. *J. Phys. Chem. C* **2009**, *113* (14), 5460–5466.
- (55) Bu, D.; Zhuang, H. Biotemplated synthesis of high specific surface area copper-doped hollow spherical titania and its photocatalytic research for degrading chlorotetracycline. *Appl. Surf. Sci.* **2013**, *265*, 677–685.
- (56) Zhang, Y.; Huang, M.; Li, F.; Zhao, H.; Wen, Z. Decoration of Cu nanowires with chemically modified TiO_2 nanoparticles for their improved photocatalytic performance. *J. Mater. Sci.* **2013**, *48*, 6728–6736.
- (57) Mao, Y.; Wong, S. S. Size- and shape-dependent transformation of nanosized titanate into analogous anatase titania nanostructures. *J. Am. Chem. Soc.* **2006**, *128* (25), 8217–8226.
- (58) Nakhate, G. G.; Nikam, V. S.; Kanade, K. G.; Arbuj, S.; Kale, B. B.; Baeg, J. O. Hydrothermally derived nanosized Ni-doped TiO_2 : A visible light driven photocatalyst for methylene blue degradation. *Mater. Chem. Phys.* **2010**, *124*, 976–981.
- (59) Khanna, P. K.; Gaikwad, S.; Adhyapak, P. V.; Singh, N.; Marimuthu, R. Synthesis and characterization of copper nanoparticles. *Mater. Lett.* **2007**, *61* (25), 4711–4714.
- (60) Ikeda, H.; Qi, Y.; Cagin, T.; Samwer, K.; Johnson, W. L.; Goddard, W. A. Strain Rate Induced Amorphization in Metallic Nanowires. *Phys. Rev. Lett.* **1999**, *82* (14), 2900–2903.
- (61) Rajagopal, K. *Engineering Physics*, 2nd ed. ed.; PHI Learning Private Limited: New Delhi, 2011; p 576.
- (62) Salavati-Niasari, M.; Davar, F. Synthesis of copper and copper(I) oxide nanoparticles by thermal decomposition of a new precursor. *Mater. Lett.* **2009**, *63* (3–4), 441–443.
- (63) Cuya Huaman, J. L.; Sato, K.; Kurita, S.; Matsumoto, T.; Jeyadevan, B. Copper nanoparticles synthesized by hydroxyl ion assisted alcohol reduction for conducting ink. *J. Mater. Chem.* **2011**, *21* (20), 7062–7069.
- (64) Ghaddar, A.; Gieraltowski, J.; Gloaguen, F. Effects of anodization and electrodeposition conditions on the growth of copper and cobalt nanostructures in aluminum oxide films. *J. Appl. Electrochem.* **2009**, *39*, 719–725.
- (65) Pootawang, P.; Saito, N.; Lee, S. Discharge time dependence of a solution plasma process for colloidal copper nanoparticle synthesis and particle characteristics. *Nanotechnology* **2013**, *24* (5), 55604–55613.
- (66) Duan, J.-L.; Liu, J.; Yao, H.-J.; Mo, D.; Hou, M.-D.; Sun, Y.-M.; Chen, Y.-F.; Zhang, L. Controlled synthesis and diameter-dependent optical properties of Cu nanowire arrays. *Mater. Sci. Eng.: B* **2008**, *147*, 57–62.
- (67) Vishlaghi, M.; Tabriz, M.; Moradi, O. Electrohydrodynamic atomization (EHDA) assisted wet chemical synthesis of nickel nanoparticles. *Mater. Res. Bull.* **2012**, *47* (7), 1666–1669.
- (68) Su, Y.; Yang, Y.; Zhang, H.; Xie, Y.; Wu, Z.; Jiang, Y.; Fukata, N.; Bando, Y.; Wang, Z. L. Enhanced photodegradation of methyl orange with TiO_2 nanoparticles using a triboelectric nanogenerator. *Nanotechnology* **2013**, *24* (29), 295401:1–6.
- (69) Wang, X. H.; Li, J.-G.; Kamiyama, H.; Moriyoshi, Y.; Ishigaki, T. Wavelength-Sensitive Photocatalytic Degradation of Methyl Orange in Aqueous Suspension over Iron(III)-doped TiO_2 Nanopowders under UV and Visible Light Irradiation. *J. Phys. Chem. B* **2006**, *110* (13), 6804–6809.
- (70) Zaleska, A. Doped- TiO_2 : A Review. *Recent Pat. Eng.* **2008**, *2*, 157–164.

- (71) Yamanaka, K.-i.; Ohwaki, T.; Morikawa, T. Charge-Carrier Dynamics in Cu- or Fe-Loaded Nitrogen-Doped TiO₂ Powder Studied by Femtosecond Diffuse Reflectance Spectroscopy. *J. Phys. Chem. C* **2013**, *117* (32), 16448–165456.
- (72) Song, K.; Zhou, J.; Bao, J.; Feng, Y. Photocatalytic Activity of (Copper, Nitrogen)-Codoped Titanium Dioxide Nanoparticles. *J. Am. Ceram. Soc.* **2008**, *91* (4), 1369–1371.
- (73) Xin, B.; Wang, P.; Ding, D.; Liu, J.; Ren, Z.; Fu, H. Effect of surface species on Cu-TiO₂ photocatalytic activity. *Appl. Surf. Sci.* **2008**, *254*, 2569–2574.
- (74) Sahu, M.; Wu, B.; Zhu, L.; Jacobson, C.; Wang, W.-N.; Jones, K.; Goyal, Y.; Tang, Y. J.; Biswas, P. Role of dopant concentration, crystal phase and particle size on microbial inactivation of Cu-doped TiO₂ nanoparticles. *Nanotechnology* **2011**, *22*, 415704- (1–9).
- (75) Mele, G.; Del Sole, R.; Vasapollo, G.; Garcia-Lopez, E.; Palmisano, L.; Schiavello, M. Photocatalytic degradation of 4-nitrophenol in aqueous suspension by using polycrystalline TiO₂ impregnated with functionalized Cu(II)-porphyrin or Cu(II)-phthalocyanine. *J. Catal.* **2003**, *217*, 334–342.
- (76) Zeng, M. Influence of TiO₂ surface properties on water pollution treatment and photocatalytic activity. *Bull. Korean Chem. Soc.* **2013**, *34* (3), 953–956.
- (77) Kemmell, M.; Pore, V.; Tupala, J.; Ritala, M.; Leskela, M. Atomic Layer Deposition of Nanostructured TiO₂ Photocatalysts via Template Approach. *Chem. Mater.* **2007**, *19*, 1816–1820.
- (78) Ziegler, K. J.; Doty, R. C.; Johnston, K. P.; Korgel, B. A. Synthesis of Organic Monolayer-Stabilized Copper Nanocrystal in Supercritical Water. *J. Am. Chem. Soc.* **2001**, *123* (32), 7797–7803.
- (79) Guerra, M. B. B.; Carapelli, R.; Miranda, K.; Nogueira, A. R. A.; Pereira-Filho, E. R. Determination of As and Sb in mineral waters by fast sequential continuous flow hydride generation atomic absorption spectrometry. *Anal. Methods* **2011**, *3*, 599–605.
- (80) Lee, W.-r.; Lim, Y. S.; Kim, S.; Jung, J.; Han, Y.-K.; Yoon, S.; Piao, L.; Kim, S.-H. Crystal-to-crystal conversion of Cu₂O nanoparticles to Cu crystals and applications in printed electronics. *J. Mater. Chem.* **2011**, *21* (19), 6928–6933.